

Crystalline particle packings on constant mean curvature (Delaunay) surfacesEnrique Bendito,¹ Mark J. Bowick,² Agustin Medina,¹ and Zhenwei Yao^{2,*}¹*Departament de Matemàtica Aplicada III, Universitat Politècnica de Catalunya, Barcelona, Spain*²*Department of Physics, Syracuse University, Syracuse, New York 13244-1130, USA*

(Received 7 May 2013; published 29 July 2013)

We investigate the structure of crystalline particle arrays on constant mean curvature (CMC) surfaces of revolution. Such curved crystals have been realized physically by creating charge-stabilized colloidal arrays on liquid capillary bridges. CMC surfaces of revolution, classified by Delaunay in 1841, include the 2-sphere, the cylinder, the vanishing mean curvature catenoid (a minimal surface), and the richer and less investigated unduloid and nodoid. We determine numerically candidate ground-state configurations for 1000 pointlike particles interacting with a pairwise-repulsive $1/r^3$ potential, with distance r measured in three-dimensional Euclidean space \mathbb{R}^3 . We mimic stretching of capillary bridges by determining the equilibrium configurations of particles arrayed on a sequence of Delaunay surfaces obtained by increasing or decreasing the height at constant volume starting from a given initial surface, either a fat cylinder or a square cylinder. In this case, the stretching process takes one through a complicated sequence of Delaunay surfaces, each with different geometrical parameters, including the aspect ratio, mean curvature, and maximal Gaussian curvature. Unduloids, catenoids, and nodoids *all* appear in this process. Defect motifs in the ground state evolve from dislocations at the boundary to dislocations in the interior to pleats and scars in the interior and then isolated sevenfold disclinations in the interior as the capillary bridge narrows at the waist (equator) and the maximal (negative) Gaussian curvature grows. We also check theoretical predictions that the isolated disclinations are present in the ground state when the surface contains a geodesic disk with integrated Gaussian curvature exceeding $-\pi/3$. Finally, we explore minimal energy configurations on sets of slices of a given Delaunay surface, and we obtain configurations and defect motifs consistent with those seen in stretching.

DOI: [10.1103/PhysRevE.88.012405](https://doi.org/10.1103/PhysRevE.88.012405)

PACS number(s): 81.10.Aj, 61.72.Lk

I. INTRODUCTION

Much has been learned in the past decade about crystalline particle packings on a wide variety of curved two-dimensional surfaces [1]. The surfaces studied include the 2-sphere (constant positive Gaussian curvature) [2–5], the 2-torus (variable positive and negative Gaussian curvature with vanishing integrated Gaussian curvature) [6–9], the paraboloid (variable Gaussian curvature and a boundary) [10,11], the Gaussian bump (positive and negative Gaussian curvature) [12–14], and the catenoid minimal surface [15–17]. Although the nature of condensed matter order on surfaces is applicable to many different physical settings, the richest comparison between theoretical and numerical predictions and experiments has been made with micron-scale colloidal systems. In these systems, solid colloidal particles self-assemble at the interface of two distinct immiscible liquids, either in particle-stabilized (Pickering) emulsions [18–20] or charge-stabilized emulsions [21,22]. The case of ordering on the 2-sphere (the surface of a ball) is realized by particles self-assembling at the surface of a droplet held perfectly spherical by surface tension [4]. The ordered configurations of particles may be imaged with confocal microscopy and the particles even manipulated with laser tweezers [23]. In charge-stabilized emulsions, particles do not even wet the surface, and so the intrinsic shape of the droplet is preserved. The natural range in size R of the droplets allows one to explore the effect of the Gaussian curvature, which varies as $1/R^2$, on the ordering. The ground

state has been found to exhibit qualitatively different types of defect arrays as the size changes [4,24]. Small droplets have 12 isolated fivefold-coordinated disclinations (5s), whereas for larger droplets the isolated 5s sprout additional chains of dislocations (a dislocation is a tightly bound disclination-antidisclination or 5-7 pair) to become 12 grain boundary scars, each of which has a net disclination charge of +1 (i.e., one excess 5) and freely terminates within the medium. Free termination of a grain boundary is possible in curved space because Bragg rows are curved along the converging geodesics of the 2-sphere, eventually healing the 30° mismatch in crystallographic axes found at the center of the grain boundary.

Recently, a very rich and flexible experimental system has been developed [15] in which charge-stabilized emulsions are created in the form of capillary bridges—these are structures in which a drop of liquid A, immersed in liquid B, spans the gap between two parallel flat glass surfaces. The surface separating the two liquids has the topology of a cylinder and necessarily has a constant mean curvature (CMC) determined by the Laplace pressure difference between the inside (A) and the outside (B) liquids. These CMC surfaces of revolution were classified in the 19th century by Charles Delaunay and come in five classes: the sphere, the cylinder, the catenoid, the unduloid, and the nodoid [25–27]. Negative Gaussian curvature is expected to give rise to quite different structures from surfaces with positive Gaussian curvature [2,15–17,28–32]. The simplest negative curvature surface is the constant negative curvature hyperbolic plane H^2 , the negative curvature analog of the 2-sphere S^2 , but the isometric embedding of H^2 as a complete subset of Euclidean 3-space is not differentiable [33] and may not be realizable physically. A geodesic triangulation

*Present address: Department of Materials Science and Engineering, Northwestern University, Evanston, IL 60208, USA.

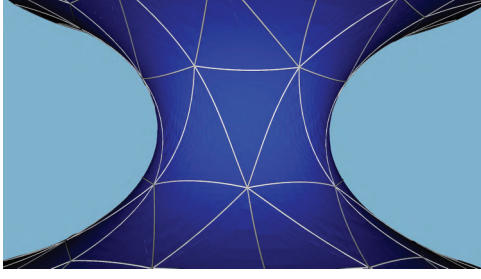


FIG. 1. (Color online) A geodesic triangulation of a negative Gaussian curvature nodoid: note the large departure of individual geodesic triangles from their Euclidean analogs where the interior angles add to π .

of a negative Gaussian curvature nodoid is shown in Fig. 1. One readily sees that the geodesic edges are diverging and that the geodesic triangles in the highly curved regions of the surface have interior angles whose sum is less than 180° —in fact some of the triangles have an interior angle sum around 140° !

In this paper, we explore the structure of the crystalline ground state of particles strictly confined to a Delaunay CMC surface and interacting with a pairwise-repulsive short-range power-law potential. Such surfaces have varying negative Gaussian curvature and are thus technically more challenging to analyze and simulate numerically. We are particularly interested in the defect structure of the ground state and how distinctive defect motifs emerge as the integrated Gaussian curvature is varied within one class of CMC surface as well as the evolution of the ground state as one quasistatically varies the manifold by increasing the height of the capillary bridge: the sequence of Delaunay surfaces studied corresponds to the physical experiment of pulling the bounding plates slowly apart or pushing them slowly together and hence stretching or compressing the capillary bridge.

II. GEOMETRY OF DELAUNAY SURFACES

Delaunay surfaces are variationally determined by being constant mean curvature surfaces of revolution with minimum lateral area and fixed volume. The characterization that most directly gives rise to a simple and useful parametrization, however, is to consider them as the surfaces of revolution whose meridians are the roulettes of the foci of the conics, that is, the curves traced by the foci of the conics as they roll on a conic tangent without slip (for a detailed study, see [34]). Besides the extreme limiting cases of the sphere and the cylinder, these surfaces are catenoids, unduloids, and nodoids, generated by the roulettes of parabolas, ellipses, and hyperbolas, respectively.

The roulette of the focus of the parabola is the catenary; the surface of revolution, the catenoid, is the best known nontrivial Delaunay surface. Its parametrization is (see Fig. 2)

$$\mathbf{x}(t, v) = \left(c \cosh\left(\frac{t}{c}\right) \cos(v), c \cosh\left(\frac{t}{c}\right) \sin(v), t \right), \quad (1)$$

where c is the radius of the waist, $v \in (0, 2\pi)$, and $t \in \mathbb{R}$.

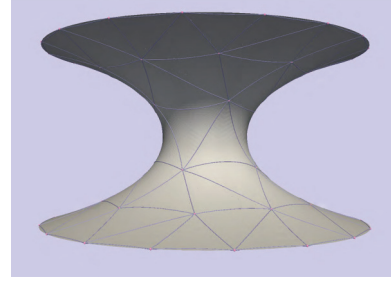


FIG. 2. (Color online) A catenoid.

The parametrization of an unduloid is given by

$$\begin{aligned} \mathbf{y}(t, v) &= (f_u(t) \cos(v), f_u(t) \sin(v), g_u(t)), \\ \text{where } f_u(t) &= \frac{b[a - c \cos(t)]}{\sqrt{a^2 - c^2 \cos^2(t)}}, \\ g_u(t) &= \int_{t_0}^t \sqrt{a^2 - c^2 \cos^2(z)} dz \\ &\quad - \frac{c \sin(t)[a - c \cos(t)]}{\sqrt{a^2 - c^2 \cos^2(t)}}, \end{aligned} \quad (2)$$

a and b are the semiaxes of the ellipse, $c = \sqrt{a^2 - b^2}$, and $v \in (0, 2\pi)$. If $t \in (-\frac{\pi}{2}, \frac{\pi}{2})$, the roulette generated by the closest focus to the tangent to the ellipse generates unduloids of the type shown in Fig. 3 (left) with negative Gaussian curvature. Taking, instead, $t \in (\frac{\pi}{2}, \frac{3\pi}{2})$, the same focus generates the unduloids with positive Gaussian curvature, such as the one shown in Fig. 3 (right). The same surfaces are obtained by using the other focus, but this time in the reverse order.

Similarly, the parametrization of a nodoid is given by

$$\begin{aligned} \mathbf{z}^1(t, v) &= (f_n^1(t) \cos(v), f_n^1(t) \sin(v), g_n^1(t)), \\ \text{where } f_n^1(t) &= \frac{b[c \cosh(t) - a]}{\sqrt{c^2 \cosh^2(t) - a^2}}, \\ g_n^1(t) &= \int_{t_0}^t \sqrt{c^2 \cosh^2(z) - a^2} dz \\ &\quad - \frac{c \sinh(t)[c \cosh(t) - a]}{\sqrt{c^2 \cosh^2(t) - a^2}}, \end{aligned} \quad (3)$$

where a and b are the semiaxes of the hyperbola, $c = \sqrt{a^2 + b^2}$, $v \in (0, 2\pi)$, and $t \in \mathbb{R}$. The expressions in (3) treat the roulette generated by the closest focus to the tangent to the hyperbola and yield nodoids with negative Gaussian curvature, as shown in Fig. 4 (left). Taking the roulette generated by the other focus yields the expressions (4) and nodoids with positive

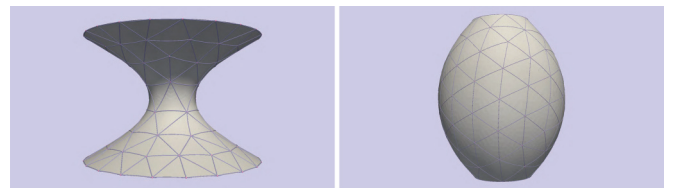


FIG. 3. (Color online) Unduloid with negative Gaussian curvature (left) and positive Gaussian curvature (right).

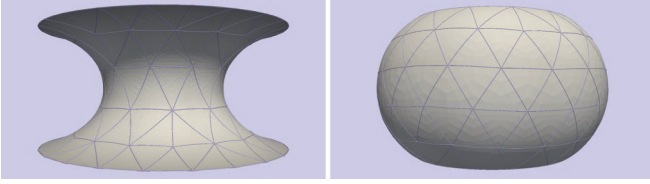


FIG. 4. (Color online) Nodoid with negative Gaussian curvature (left) and positive Gaussian curvature (right).

Gaussian curvature, as illustrated in Fig. 4 (right),

$$\begin{aligned} z^2(t, v) &= (f_n^2(t) \cos(v), f_n^2(t) \sin(v), g_n^2(t)) \\ \text{where } f_n^2(t) &= \frac{b[c \cosh(t) + a]}{\sqrt{c^2 \cosh^2(t) - a^2}}, \\ g_n^2(t) &= \int_{t_0}^t \sqrt{c^2 \cosh^2(z) - a^2} dz \\ &\quad - \frac{c \sinh(t)[c \cosh(t) + a]}{\sqrt{c^2 \cosh^2(t) - a^2}}. \end{aligned} \quad (4)$$

All the fundamental properties of the Delaunay surfaces can be obtained easily using these parametrizations. In particular, the mean curvature of catenoids, unduloids, and nodoids is given by

$$H_c = 0, \quad H_u = \frac{1}{2a}, \quad H_n^1 = H_n^2 = \frac{-1}{2a}, \quad (5)$$

respectively, where a is the semimajor axis of the related conic. The Gaussian curvatures of catenoids, unduloids, and nodoids are given by

$$\begin{aligned} K_c &= \frac{-1}{c^2 \cosh^4(t)}, & K_u &= \frac{-c \cos(t)}{a[a - c \cos(t)]^2}, \\ K_n^1 &= \frac{-c \cosh(t)}{a[c \cosh(t) - a]^2}, & K_n^2 &= \frac{c \cosh(t)}{a[c \cosh(t) + a]^2}. \end{aligned} \quad (6)$$

III. NUMERICAL SIMULATION: FINDING A MINIMUM ENERGY CONFIGURATION ON A DELAUNAY SURFACE

To determine candidate minimum energy configurations, we use the forces method [35,36]. The basic structure of the forces method is classical and explained in detail in [36]. For completeness, we give a brief description here. It can be viewed as a local relaxation-gradientlike descent algorithm where each step consists of finding the update direction and the step size in a predefined way. It consists of four steps:

- (i) Choose a certain number of particles and an initial configuration for them.
- (ii) Update the positions of the particles in three-dimensional space.
- (iii) Project the positions on the surface.
- (iv) Repeat steps (ii) and (iii) until a given threshold is reached.

Briefly, these are as follows:

Initial configuration. The initial configuration is chosen to be as uniformly distributed on the given Delaunay surface as possible, with the restriction that the particles are not near the two boundaries. Many independent runs (order 10) are made

starting from different initial configurations, and the lowest energy configuration is selected.

Update and projection. For one particle,

$$\hat{x}^{k+1} = \vec{x}^k + \lambda_k \vec{w}^k,$$

where \vec{x}^k , \vec{w}^k , and λ_k are the position, update direction, and step size at the k th step, respectively. \hat{x}^{k+1} would be the new location of the particle if this location were on the surface. Since it is generically off the surface after the update, the actual position \vec{x}^{k+1} is obtained by projecting \hat{x}^{k+1} onto the surface.

The update direction is in the direction of the net force on the particle following from the gradient of the potential. In this paper, as noted before, we use a $1/r^3$ power-law potential. For a system of N charge 1 particles, $\vec{x}_i \in \mathbb{R}^3, i = 1, \dots, N$, the potential energy is then given by $\mathcal{I}_N = \frac{1}{2} \sum_{i=1}^N V_i$, where $V_i = \sum_{j \neq i}^N \frac{1}{|\vec{x}_i - \vec{x}_j|^3}$ is the potential created at \vec{x}_i by all the other particles. We denote by \vec{F}_i minus the gradient of V_i in terms of the position of the i th particle.

If the particles lie on a regular surface S , then equilibrium is reached when the component of \vec{F}_i tangential to S , \vec{F}_i^T , vanishes at \vec{x}_i . Then we choose $w = (\vec{w}_1, \dots, \vec{w}_N)$ as the step direction, where $\vec{w}_i = \frac{\vec{F}_i^T}{|\vec{F}_i^T|}$ (we normalize by the maximum force). The magnitude of the step size is then $\lambda_k(\vec{x}_i) = d(\min_{\substack{1 \leq j \leq N \\ j \neq i}} \{|\vec{x}_i^k - \vec{x}_j^k|\})^2$, where the coefficient d is a constant positive scalar. The existence of a minimum distance between particles makes it possible to adjust the step size to most efficiently access the various configurations that arise during the iterative process. The error at iteration k is $w_{\max} = \max_{1 \leq i \leq N} |\vec{w}_i|$. The algorithm stops when w_{\max} reaches a certain prescribed threshold value $\varepsilon > 0$.

The 1000 particle simulations are performed on an Intel core i7 processor at a speed of 36.5 iterations/s. We simulate 23 distinct particle systems in all requiring a total of 5.522×10^6 iterations for a total CPU time of 42 h.¹

IV. CONSTANT VOLUME RESULTS

In this section, we analyze the evolution of defect motifs on a capillary bridge as it is stretched while preserving the volume and the contact area with both bounding parallel flat plates (corresponding to the boundary disks of the Delaunay surface). At each stage of stretching, the capillary bridge is a distinct Delaunay surface with different mean and Gaussian curvatures. Thus, in the experimental setting, the particles must continuously reequilibrate to a new ground state. Numerically, we minimize the energy on each Delaunay surface separately. This analysis allows one to explore the structure of an entire sequence of Delaunay surfaces, one for each stage of the stretch. We study two types of constant volume stretching: one starts from a fat cylindrical capillary bridge and the other from a square cylindrical capillary bridge.

¹Coordinates and energies for the configurations analyzed in this paper may be obtained by contacting Mark Bowick (bowick@phy.syr.edu).

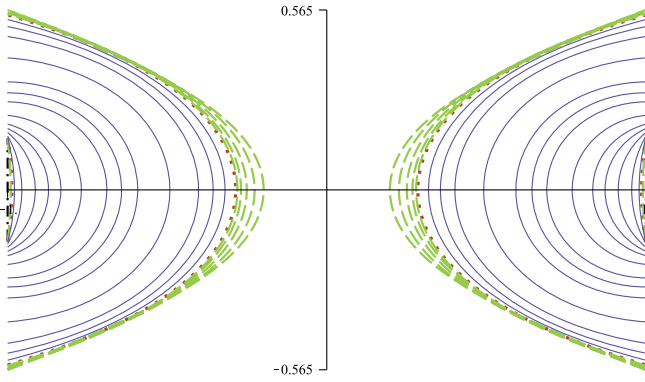


FIG. 5. (Color online) Representative members of the family of surfaces obtained by stretching a fat cylinder. From the outside in: cylinder (black, dashed lines at the utmost left and right sides), unduloids (green, dashed lines at the utmost left and right sides), catenoid (red, dotted lines at the utmost left and right sides), nodoids (blue, solid), catenoid (red, dotted lines near the neck), and unduloids (green, dashed lines near the neck).

A. Stretching from an initial fat cylindrical capillary bridge

The initial fat cylinder has a contact radius $r_c = 1$ and height $h = 1/\pi$, so both the volume and the aspect ratio [the ratio ρ of the radius of the surface at an equatorial plane (waist) to the radius of the contact disk at the plates] are unity. In our numerical study, starting from a fat cylindrical capillary bridge yields a rich family of surfaces that begins with the cylinder and subsequently deforms to a series of unduloids, the catenoid, and then a series of nodoids. Thus all the classes of Delaunay surfaces, apart from the well-studied 2-sphere which can be generated by other simpler means, are explored in this single process. Minimum energy configurations for charged particles interacting via a Yukawa potential and confined to Delaunay surfaces were obtained in [32], but only for catenoids and unduloids. As is clear from Fig. 5, the predominant surfaces in stretching are nodoids. The proper treatment of nodoids is therefore essential to a comparison with the experiments of Ref. [15]. Planar sections that contain the common revolution axis of several surfaces from this family are shown in Fig. 5. The final unduloid has an aspect ratio $\rho = 0.198$.

We obtain minimum energy states for $N = 1000$ particles interacting via a pairwise-repulsive $1/r^3$ potential. Short-range potentials (decaying faster than $1/r^2$) produce more uniform ground-state configurations because long-range potentials (decaying slower than $1/r^2$) drive particles to the boundary

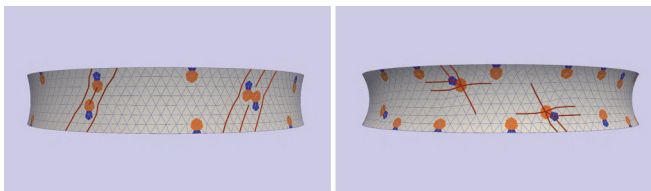


FIG. 6. (Color online) Left: Equilibrium configuration for a nodoid with aspect ratio $\rho = 0.97$. Some Bragg rows are highlighted in white to illustrate the insertion of half-lines of particles defining a dislocation. Right: Equilibrium configuration for a nodoid with $\rho = 0.95$. Some dislocations are parallel to the nodoid’s boundary.

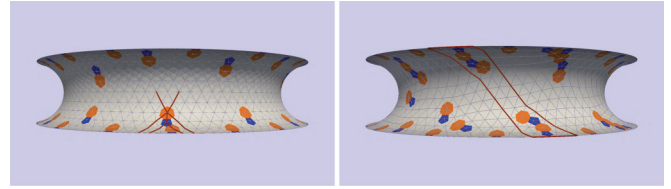


FIG. 7. (Color online) Left: Appearance of pleats at aspect ratio $\rho = 0.81$. The distortion of the crystallographic rows corresponds to that of a chain of dislocations. Right: at $\rho = 0.78$, pleats and dislocations begin to proliferate.

circles to maximize the average separation. This can lead to defect structures that are influenced by the boundary. While of intrinsic interest as a boundary-driven phenomenon, this is not our primary focus in this paper. We found that long-range effects may also be reduced, but not eliminated, by adding a line of neutralizing charge along the central axis of the surface. Here we focus on the role of variable Gaussian curvature in the interior of Delaunay surfaces.

Various defect motifs emerge as the capillary bridge becomes higher and thinner (decreasing aspect ratio with our definition). Basically, we identify the following sequence: at $\rho = 0.984$, individual dislocations (tightly bound 5-7 pairs) appear at the boundary, resulting from the repulsion between dislocations of identical orientation.

As ρ decreases, these dislocations migrate to the interior of the surface and occasionally form multiple dislocation clusters. In Fig. 6 (left, right), we show minimum energy configurations for $\rho = 0.97$ and 0.95 . The dual pentagons and heptagons shown here are obtained by first performing a Delaunay triangulation of the configuration and then connecting the barycenters of adjacent triangles. In Fig. 6 (left), we also highlight the Bragg rows on each side of two pairs of dislocations so that one can see the removal (insertion) of a half-line of particles characteristic of a dislocation (antidislocation). In Fig. 6 (right), we highlight the Bragg rows surrounding two dislocations oriented almost tangentially to the boundary (and thus with Burgers vector almost parallel to the boundary). At $\rho = 0.81$, pleats appear attached to the boundary, as shown in Fig. 7 (left). Pleats are neutral grain boundaries with a fivefold disclination at one end and a sevenfold disclination at the other end. A pleat can freely terminate at one or both ends and so they are easy to recognize. Below $\rho = 0.78$, pleats and dislocations proliferate both in the interior and at the boundaries [see Fig. 7 (right)].

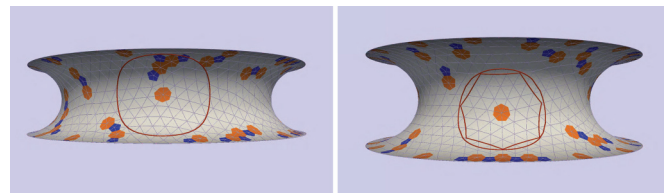


FIG. 8. (Color online) Left: Nodoid with aspect ratio $\rho = 0.774$. Note the appearance of an isolated 7-disclination. The white circle is the geodesic circle centered on the 7 that encloses an integrated Gaussian curvature of $-\pi/3$. Right: Nodoid with aspect ratio $\rho = 0.64$. The geodesic circle, centered on the 7, that encloses a $-\pi/3$ integrated Gaussian curvature (white circle) is compared to its lattice analog.

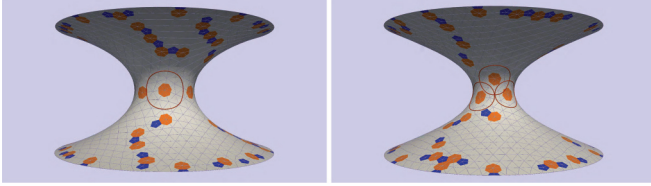


FIG. 9. (Color online) Left: Catenoid (vanishing mean curvature) with aspect ratio $\rho = 0.28$. Note the appearance of several isolated 7s in the region of the waist. The white contour is that of a geodesic circle centered on the 7 inside and enclosing an integrated Gaussian curvature of $-\frac{\pi}{3}$. Right: Unduloid with aspect ratio $\rho = 0.198$. Three geodesic disks enclosing an integrated Gaussian curvature of $-\frac{\pi}{3}$ are also shown.

At $\rho = 0.774$, one sees isolated sevenfold disclinations (7s). In the figures these are seen clearly in the form of their dual heptagons. This is the true hallmark of the prevailing negative Gaussian curvature in the interior of the surface. Sevenfold disclinations may arise by the unbinding of a 7 from a pleat, which typically ends with a 7 oriented toward the central interior of the surface. Indeed there are usually compensating scars with a net positive disclination charge near an isolated 7 in this regime of aspect ratios. As the negative Gaussian curvature increases, however, isolated 7s are typically farther away from the positive scars that compensate them topologically.

In Fig. 8 (left), we show a minimal energy configuration, with aspect ratio $\rho = 0.774$, containing an isolated sevenfold disclination. We also show the geodesic circle, Γ , with radius $r = 0.293$, which is the boundary of a disk D whose integrated Gaussian curvature is $-\frac{\pi}{3}$. Γ was determined by constructing a geodesic polygon with enough edges that the integrated curvature coincides with the total exterior angle deficit and applying the Gauss-Bonnet theorem

$$\int_D K dA + \sum_i \gamma_i = 2\pi, \quad (7)$$

where K is the Gaussian curvature and γ_i is the exterior angle deficit at vertex i . Since disclinations naturally couple to Gaussian curvature in the effective Hamiltonian that controls

their energetics [1,2,15,16], a natural criterion for the ground state to admit a defect with a net -1 disclination charge is that there be a domain of the surface, centered on the defect, with integrated Gaussian curvature matching the disclination charge $-\pi/3$.

In Fig. 8 (right), we show a configuration, with aspect ratio $\rho = 0.64$, containing a completely isolated 7 along with the geodesic circle centered on the 7 and enclosing an integrated Gaussian curvature of $-\frac{\pi}{3}$. We have also inscribed a seven-sided geodesic polygon as determined by the triangulation. The exterior angles grow from $2\pi/7$ at the sevenfold disclination to $2\pi/6$ at the inscribed geodesic heptagon. This nodoid has a vanishing contact angle at the boundary, corresponding to complete wetting of the capillary bridge at the plates; it corresponds to the nodoid with parameter t covering all \mathbb{R} . For a smaller aspect ratio, the contact angle grows to a maximum of 22° .

As the capillary bridge is stretched to have a very narrow waist (the equatorial section $t = 0$ of the Delaunay surface) with large negative maximal Gaussian curvature, we observe a proliferation of sevenfold disclination defects (heptagons). Two examples are displayed in Fig. 9 (left, right). In both configurations there are a total of 11 isolated 7s plus scars, which have the same net disclination charge. The 7s preferentially occupy the waist of the capillary bridge, whereas scars and pleats are found throughout the surface.

The sequence of defect motifs revealed by our simulations conforms remarkably closely to that found experimentally in [15] (see, in particular, their Fig. 4). The initial compressed bridge is free of defects. As the bridge is stretched, both experimentally and numerically, one observes the appearance of dislocations, neutral disclination dipoles, polarized with the sevenfold disclinations toward the maximally negatively curved neck (see Fig. 6 and Fig. 4(i) of [15]). Further stretching leads to the appearance of pleats (see Fig. 7 and Fig. 4(j) of [15]). Finally, yet more stretching leads to the appearance of isolated sevenfold disclinations and scars (see Fig. 8 and Fig. 4(k) of [15]). These comparisons were also noted in [32], but we note that all the stretched manifolds displaying defects are nodoids (as clearly established in Fig. 5) whereas the simulations in [32] are only for catenoids and unduloids.

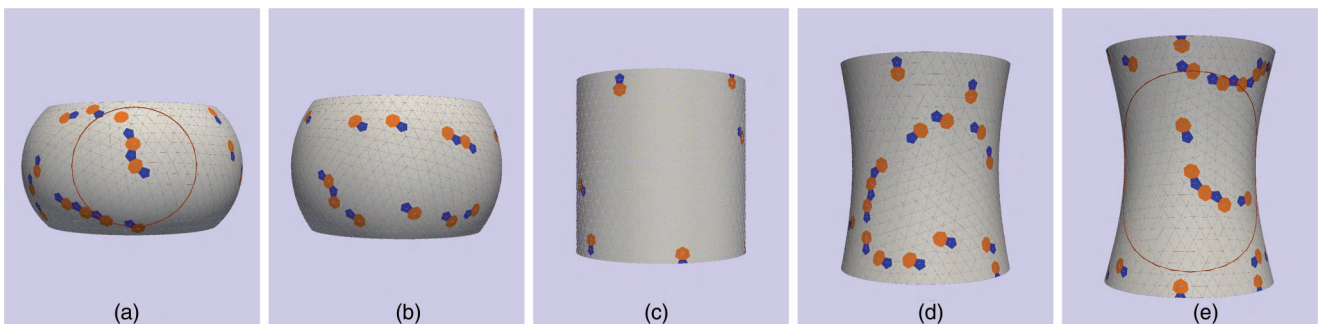


FIG. 10. (Color online) Square cylindrical capillary bridges. (a) Positive Gaussian curvature nodoid with aspect ratio $\rho = 1.30$. Observe the encircled 5-7-5-7-5 scar separated by a lattice spacing from an isolated 7. The geodesic disk enclosed by the circle has integrated Gaussian curvature $\frac{\pi}{3}$. (b) Positive Gaussian curvature unduloid with aspect ratio $\rho = 1.24$. Observe isolated dislocations and pleats. (c) Null Gaussian curvature cylinder with aspect ratio $\rho = 1$. (d) Negative Gaussian curvature nodoid with aspect ratio $\rho = 0.86$. Note the long 7-5-7-5-7-5 pleat situated left center. (e) Negative Gaussian curvature unduloid with aspect ratio $\rho = 0.77$. Observe the prominent 7-5-7-5-7-5 scar. The geodesic disk enclosed by the circle has integrated Gaussian curvature $-\frac{\pi}{3}$.

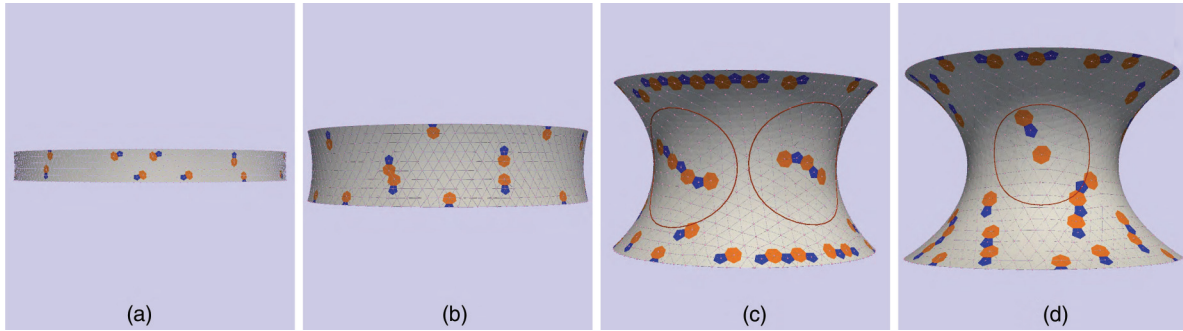


FIG. 11. (Color online) Different slices of the nodoid with parameters $a = 0.5$ and $b = 0.1$. (a) $t_{\max} = 0.02$, (b) $t_{\max} = 0.05$, (c) $t_{\max} = 0.2$, and (d) $t_{\max} = 0.3$.

B. Stretching from an initial square cylindrical capillary bridge

In this section, we discuss the appearance of defects upon stretching through another family of Delaunay surfaces preserving volume and contact radius. This family is generated by starting from a positive Gaussian curvature nodoid with an aspect ratio $\rho = 1.30$ and is designed to pass through the square cylindrical capillary bridge with $r_c = 1$ and $h = 2$ (aspect ratio $\rho = 1$). It terminates in an unduloid with an aspect ratio $\rho = 0.77$. Representative configurations for this sequence are shown in Fig. 10. The central cylinder exhibits very few defects. Increasing or decreasing the aspect ratio leads first to the appearance of pleats and then to longer pleats and scars. Geodesic disks with total curvature $\pm \frac{\pi}{3}$ are shown surrounding scars and are completely contained in the interior of the surface. Note that the defect structure in Fig. 10(a) is a pleat with the top sevenfold disclination separated by one lattice spacing from the rest of the pleat.

V. MINIMUM ENERGY CONFIGURATIONS ON SLICES

For an isolated sevenfold disclination (heptagon) to be present in minimum energy configurations of crystalline arrays on a negative curvature surface, a reasonable criterion is that the integrated Gaussian curvature over the geodesic disk centered at the disclination be more negative than $-\frac{\pi}{3}$, the deficit angle corresponding to the topological charge of a sevenfold disclination [1]. To check that it is the integral of the Gaussian curvature, instead of the Gaussian curvature itself, that determines the character of defect motifs, we examine minimum energy configurations on slices of a given

Delaunay surface with steadily increasing values of t_{\max} , the maximal value of the meridian coordinate t . Each slice has t spanning the interval $[-t_{\max}, t_{\max}]$. The shape of a nodoid is completely determined by the parameters a and b . We merely restrict to a growing set of slices by varying t_{\max} . The first surface we investigate is the nodoid with $a = 0.5$ and $b = 0.1$. This capillary bridge has maximal Gaussian curvature at the $t = 0$ waist (equator) of $K(0) = -10401$. In Fig. 11(a), we take a slice with $t_{\max} = 0.02$ and the behavior is completely equivalent to a cylinder. For completeness, we note that this surface encloses a volume $V = 6.11 \times 10^{-7}$ and has a lateral area $A = 1.23 \times 10^{-4}$ and an equilibrium potential energy $E = 1.17 \times 10^{13}$.

In Fig. 11(b), we show a slice with $t_{\max} = 0.05$. For this slice, dislocations are found in the interior just as in the case of stretching within the fat cylinder family. The evolution of defect motifs continues with the appearance of pleats and, in Fig. 11(c), where $t_{\max} = 0.2$, disclination charge -1 scars sitting inside disks of integrated Gaussian curvature $-\frac{\pi}{3}$. The first appearance of an isolated sevenfold disclination (heptagon) is for a slice with $t_{\max} = 0.3$. In Fig. 11(d), we show the geodesic disk of geodesic radius $r = 0.0061$, the same value as in the previous slice, because the surfaces are the same except for their height. This last surface encloses a volume of $V = 1.17 \times 10^{-5}$ and has a lateral area $A = 3.39 \times 10^{-3}$.

As we increase the parameter b , the Gaussian curvature in the waist is strongly reduced and yet the sequence of defect motifs is essentially the same. To be concrete, we show the family of slices with $a = 0.5$ and $b = 0.4$. Now the Gaussian curvature in the waist is $K(0) = -65$.

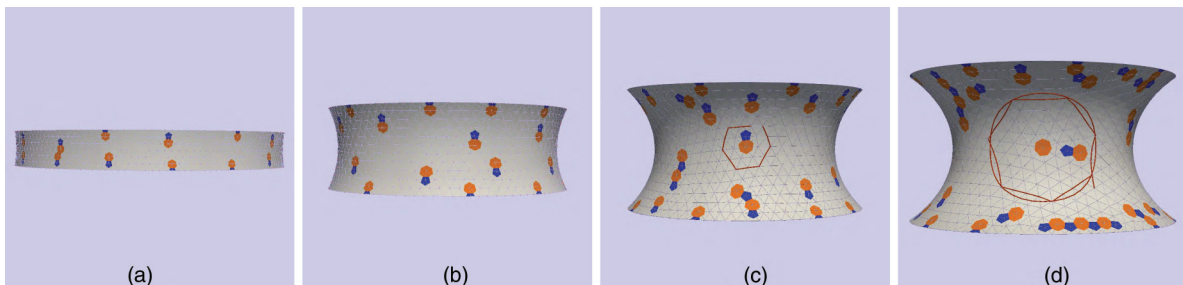


FIG. 12. (Color online) Different slices of the nodoid with $a = 0.5$ and $b = 0.4$. (a) $t_{\max} = 0.1$, (b) $t_{\max} = 0.3$, (c) $t_{\max} = 0.6$, and (d) $t_{\max} = 0.8$.

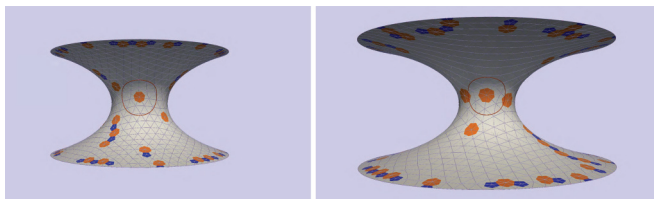


FIG. 13. (Color online) Left: nodoid with $a = 0.5$, $b = 0.1$, and $t_{\max} = 0.6$ with a geodesic disk of total curvature $-\frac{\pi}{3}$ in one of the isolated $7s$ in the waist. Right: The same nodoid but with a larger slice, now $t_{\max} = 0.9$.

In Fig. 12(a), we display a slice with $t_{\max} = 0.1$ and the pattern is again equivalent to a cylinder. Its volume is 2.17×10^{-3} and the lateral area is 3.1×10^{-2} . In Fig. 12(b), we again observe the formation of dislocations in the interior. In Fig. 12(c), we have enclosed a dislocation with a polygon to show the associated Burgers' vector. In Fig. 12(d), we see an isolated sevenfold disclination with a nearby dislocation.

Finally, in Fig. 13 we include the evolution of defects for the nodoid with parameters $a = 0.5$ and $b = 0.1$, when t_{\max} increases and the slices contain most of the nodoid. In both cases there are 11 total defects counting isolated $7s$ and scars. In Fig. 13 (right), the isolated $7s$ are more concentrated in the waist.

Thus we find the full range of phenomena explored experimentally in [15] by simulating the full range of Delaunay

surfaces generated in stretching. We emphasize that catenoids and unduloids alone are insufficient in making a proper comparison with experiment [32] since the majority of surfaces encountered in stretching are nodoids with negative mean curvature as opposed to the positive mean curvature of unduloids.

The presence of isolated sevenfold disclinations (or equivalently their dual heptagons) or scars in the ground state offers new possibilities for supramolecular chemistry via functionalization of crystalline arrays on these surfaces, provided one can chemically detect the sevenfold disclination (or scars) and attach ligands there just as smectic disclinations are functionalized by place-exchange reactions for nanoparticles coated with an equal mixture of short and long chain alkanethiols in the work of DeVries *et al.* [37]. Isolated sevenfold disclinations, scars, and pleats may also be sources of material weakness or perhaps improved performance through capturing material dislocations and thus limiting plastic deformation.

ACKNOWLEDGMENTS

This research work was partly supported by the Spanish Research Council under project MTM2010-19660, by the National Science Foundation through Award No. DMR-0808812, and by the Soft Matter Program at Syracuse University. M.J.B. would like to thank David Nelson and William Irvine for many stimulating discussions on the nature of condensed matter order on capillary bridges over a period of several years.

-
- [1] M. J. Bowick and L. Giomi, *Adv. Phys.* **58**, 449 (2009).
 - [2] M. J. Bowick, D. R. Nelson, and A. Travesset, *Phys. Rev. B* **62**, 8738 (2000).
 - [3] M. Bowick, A. Cacciuto, D. R. Nelson, and A. Travesset, *Phys. Rev. Lett.* **89**, 185502 (2002).
 - [4] A. Bausch, M. Bowick, A. Cacciuto, A. Dinsmore, M. Hsu, D. Nelson, M. Nikolaidis, A. Travesset, and D. Weitz, *Science* **299**, 1716 (2003).
 - [5] M. Bowick, H. Shin, and A. Travesset, *Phys. Rev. E* **75**, 021404 (2007).
 - [6] L. Giomi and M. J. Bowick, *Phys. Rev. E* **78**, 010601(R) (2008).
 - [7] L. Giomi and M. J. Bowick, *Eur. Phys. J. E* **27**, 275 (2008).
 - [8] E. Páram and A. Fernández-Nieves, *Phys. Rev. Lett.* **102**, 234501 (2009).
 - [9] Z. Yao and M. J. Bowick, *Eur. Phys. J. E* **34**, 32 (2011).
 - [10] L. Giomi and M. Bowick, *Phys. Rev. B* **76**, 054106 (2007).
 - [11] M. J. Bowick, L. Giomi, H. Shin, and C. K. Thomas, *Phys. Rev. E* **77**, 021602 (2008).
 - [12] J.-F. Sadoc and J. Charvolin, *Acta Crystallogr. Sec. A* **45**, 10 (1989).
 - [13] V. Vitelli and D. R. Nelson, *Phys. Rev. E* **70**, 051105 (2004).
 - [14] V. Vitelli, J. B. Lucks, and D. R. Nelson, *Proc. Natl. Acad. Sci. USA* **103**, 12323 (2006).
 - [15] W. T. M. Irvine, V. Vitelli, and P. M. Chaikin, *Nature (London)* **468**, 947 (2010).
 - [16] M. J. Bowick and Z. Yao, *Europhys. Lett.* **93**, 36001 (2011).
 - [17] W. T. M. Irvine and V. Vitelli, *Soft Matter* **8**, 10123 (2012).
 - [18] B. P. Binks and T. S. Horozov, *Colloidal Particles at Liquid Interfaces* (Cambridge University Press, Cambridge, UK, 2006).
 - [19] S. Pickering, *J. Chem. Soc.* **91**, 2001 (1907).
 - [20] A. Dinsmore, M. F. Hsu, M. Nikolaidis, M. Marquez, A. Bausch, and D. Weitz, *Science* **298**, 1006 (2002).
 - [21] M. E. Leunissen, A. van Blaaderen, A. D. Hollingsworth, M. T. Sullivan, and P. M. Chaikin, *Proc. Natl. Acad. Sci. USA* **104**, 2585 (2007).
 - [22] M. E. Leunissen, J. Zwanikken, R. van Roij, P. M. Chaikin, and A. van Blaaderen, *Phys. Chem. Chem. Phys.* **9**, 6405 (2007).
 - [23] W. T. M. Irvine, M. J. Bowick, and P. M. Chaikin, *Nat. Mater.* **11**, 948 (2012).
 - [24] M. J. Bowick, A. Cacciuto, D. R. Nelson, and A. Travesset, *Phys. Rev. B* **73**, 024115 (2006).
 - [25] J. Eells, *Math. Intell.* **9**, 53 (1987).
 - [26] C. Delaunay, *J. Math. Pures Appl. Sér. 1* **6**, 309 (1841).
 - [27] M. Sturm, *J. Math. Pures Appl. Sér. 1* **6**, 315 (1841).
 - [28] D. R. Nelson, *Phys. Rev. B* **28**, 5515 (1983).
 - [29] M. Rubinstein and D. R. Nelson, *Phys. Rev. B* **28**, 6377 (1983).
 - [30] G. Tarjus, F. Sausset, and P. Viot, *Adv. Chem. Phys.* **148**, 251 (2012).
 - [31] F. Sausset, G. Tarjus, and D. R. Nelson, *Phys. Rev. E* **81**, 031504 (2010).
 - [32] H. Kusumaatmaja and D. J. Wales, *Phys. Rev. Lett.* **110**, 165502 (2013).

- [33] D. W. Henderson and D. Taimina, *Math. Intell.* **23**, 17 (2001).
- [34] E. Bendito, M. Bowick, and A. Medina, [arXiv:1305.5681](https://arxiv.org/abs/1305.5681).
- [35] E. Bendito, A. Carmona, A. M. Encinas, and J. M. Gesto, *J. Comput. Phys.* **225**, 2354 (2007).
- [36] E. Bendito, A. Carmona, A. Encinas, J. Gesto, A. Gómez, C. Mouriño, and M. Sánchez, *J. Comput. Phys.* **228**, 3288 (2009).
- [37] G. A. DeVries, M. Brunnbauer, Y. Hu, A. M. Jackson, B. Long, B. T. Neltner, O. Uzun, B. H. Wunsch, and F. Stellacci, *Science* **315**, 358 (2007).